Teleseisms and microseisms on an ocean-bottom distributed acoustic sensing array

Ethan F. Williams[1,2], Maria R. Fernández-Ruiz[3], Regina Magalhaes[3],

Roel Vanthillo[4], Zhongwen Zhan[2], Miguel González-Herráez[3],

Hugo F. Martins[5]

May 30, 2019

Abstract

Sparse seismic instrumentation in the oceans limits our understanding of deep Earth dynamics and submarine earthquakes. Distributed acoustic sensing (DAS), an emerging technology that converts optical fiber to seismic sensors, allows us to leverage pre-existing submarine telecommunication cables for seismic monitoring. Here we report observations of a teleseismic earthquake, local surface gravity waves, and microseism along a 4192-sensor ocean-bottom DAS array offshore Belgium. We successfully recover P- and S-wave phases from the 2018-08-19 $M_w 8.2$ Fiji deep earthquake in the 0.01-1 Hz frequency band. We also observe in-situ how opposing groups of ocean surface gravity waves generate double-frequency seismic Scholte waves, as described by the Longuet-Higgins theory of microseism generation. These results suggest great potential of DAS in next-generation submarine seismic networks.

1   Introduction

One of the greatest outstanding challenges in seismology is the sparsity of instrumentation across Earth's oceans (Lay, 2009, McGuire et al., 2017). Poor spatial coverage results in biases and low-resolution regions in global tomography models as well as significant location uncertainty for offshore seismicity. Modern ocean-bottom seismometers (OBS) generally fall into two categories: short-period instruments (∼1-5 Hz), which can record for up to a month or more, and long-period or broadband

---

[1]Corresponding Author: `efwillia@gps.caltech.edu`

[2]Seismological Laboratory, California Institute of Technology, 1200 E. California Blvd., Pasadena, CA 91125-2100, USA

[3]Department of Electronics, University of Alcalá, Polytechnic School, Alcalá de Henares, Madrid 28871, Spain

[4]Marlinks, Sint-Maartenstraat 5, 3000 Leuven, Belgium

[5]Instituto de Óptica, CSIC, 28006 Madrid, Spain

instruments (BBOBS), which often employ the same sensors as terrestrial broadband seismic stations and can operate for as long as two years (Suetsugu and Shiobara, 2014). Whereas short-period instruments are primarily used in active-source experiments, BBOBS are ideal for passive-source experiments and have been used for tomographic studies, earthquake location, and ocean wave monitoring among numerous other applications (e.g. Forsyth et al., 1998; Toomey et al., 1998; Webb et al., 2001; Dolenc et al., 2005; Suetsugu et al., 2005; Shinohara et al., 2011; Ito et al., 2012; Sugioka et al., 2012; Tan et al., 2016). However, BBOBS are expensive and limited by data telemetry and battery life except in near-shore environments (Suetsugu and Shiobara, 2014). Recent work has explored several alternatives to conventional BBOBS for offshore seismic monitoring, including free-floating robots equipped with hydrophones (Hello et al., 2011), moored surface buoys or autonomous surface vehicles for satellite telemetry acoustically linked to BBOBS (Frye et al., 2005; Berger et al., 2016), and cabled arrays of broadband sensors (Goertz and Wuestefeld, 2018). Recently, Marra et al. [2018] applied laser interferometry to convert long ocean-bottom telecommunications optical fiber links into seismic strainmeters. This work is particularly promising because it would enable the >1 million km of pre-existing transoceanic telecommunications cables to be repurposed as seismic sensors, permitting rapid detection and location of earthquakes throughout the world's ocean basins. Unfortunately, the particular technique in Marra et al. [2018] is limited to measuring propagation delays integrated across an entire cable length, resulting in a single seismograph with equivalent station location uncertainty on the order of 1 km and complicated instrument response.

Distributed acoustic sensing (DAS) is an emerging technology with strong potential to form the core of next-generation submarine seismic monitoring infrastructure. A DAS interrogator unit probes a fiber-optic cable with a coherent laser pulse and measures changes in the phase of the returning optical backscatter time-series. Optical phase shifts between pulses are proportional to longitudinal strain in the fiber and can be mapped into the finite, distributed strain across a fiber segment (termed gauge length) by integration. Applying DAS technology to a fiber-optic cable effectively converts the cable into a seismic recording array with thousands of single-component channels, real-time data telemetry, and unlimited deployment duration as long as the DAS unit is powered. For about a decade, DAS has been successfully utilized in boreholes for active-source seismic profiling (e.g. Mestayer et al., 2011; Mateeva et al., 2012; Parker et al., 2014). Recent work with onshore trenched or conduit-installed horizontal fibers has demonstrated the ability of DAS arrays to record earthquakes and other seismic signals at local to teleseismic distances with high waveform fidelity (Lindsey et al., 2017; Jousset et al., 2018; Li and Zhan, 2018; Wang et al., 2018; Ajo-Franklin et al., 2019; Yu et al., 2019). In this letter, we demonstrate that submarine horizontal DAS arrays utilizing pre-existing ocean-bottom fiber-optic cables are similarly effective for seismological studies and can also record pressure perturbations from

ocean wave phenomena. We report our observation of body waves from the 2018-08-19 $M_w8.2$ Fiji deep earthquake on an ocean-bottom DAS array offshore Zeebrugge, Belgium. We then examine ocean surface gravity waves and associated seismic modes directly observed on the array, which we interpret as evidence of in-situ microseism generation. Finally, we discuss implications for future DAS deployments in marine settings.

2   Results

Passively recording during August 2018, the Belgium DAS array (BDASA) occupied a pre-existing ocean-bottom fiber-optic cable in the Southern Bight of the North Sea offshore Zeebrugge, Belgium. The fiber was originally installed to monitor a power cable for the Belwind Offshore Wind Farm. A chirped-pulse DAS system built and installed by the University of Alcala (Pastor-Graells et al., 2016) continuously interrogated a 42-km near-shore segment of the fiber with channel spacing of 10 m, creating 4192 simultaneously recording seismic sensors (Fig. 1) (see Section 4). The cable is buried between 0.5 and 3.5 m below the seafloor in water depths shallower than 40 m. The conduit housing the buried cable is mechanically coupled to the surrounding sediment, making the array sensitive to solid earth strains like earthquake wavefields and microseism noise. Meanwhile, pore fluid surrounding the cable is close to hydrodynamic equilibrium with the ocean above, so pressure perturbations and poroelastic strains from ocean waves are also recorded. The cable geometry is approximately straight over four 10-km segments and is flat or shallowly dipping, except for a steep channel around 10 km and two ∼15 m bathymetric ridges at ∼30 and 40 km from the coast (Fig. 1A).

2.1   2018-08-19 $M_w8.2$ Fiji deep earthquake

On August 19, 2018, a $M_w8.2$ deep earthquake occured in the Fiji-Tonga area, and strong teleseismic body waves were captured on global seismic networks, including the BDASA (Fig. 1B). Teleseisms arrived from an epicentral distance of 146.7^o (>16,300 km), at a back azimuth of 358.5^o (27.6^o oblique to the mean fiber azimuth of 330.9^o). In this section, we analyze a 1-hr record from the full array containing the principal body wave phases. Because the 2018-08-19 Fiji event occurred at a depth of 600 km, only weak surface waves were excited and hence could not be analyzed.

In the time-domain, raw strain records from the BDASA are uninterpretable due to the superposition of several coherent signals with incoherent noise from sources such as temperature drift (Fig. S1). A 2D Fast Fourier Transform to the frequency-wavenumber (f-k) domain allows identification and separation of coherent seismic and oceanic signals based on their characteristic phase velocities (Fig. 2). F-k domain analysis of the raw BDASA data is possible here because the chirped-pulse DAS system exhibits negligible
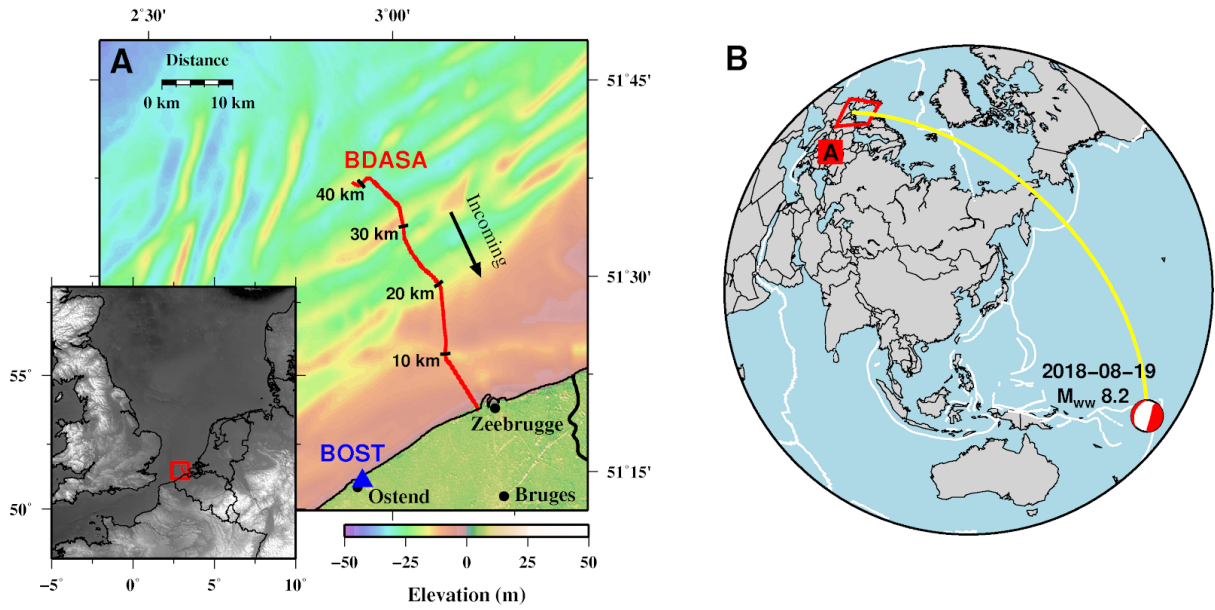
Figure 1: **Array location** (A) Local map showing the location Belgium DAS Array (BDASA, red line) and nearby broadband station BOST (blue triangle), with a regional map inset. (B) World map showing the location of the array (red box), the GCMT solution for the 2018-08-19 M8.2 Fiji deep earthquake, and great circle path between the earthquake epicenter and the array (yellow).
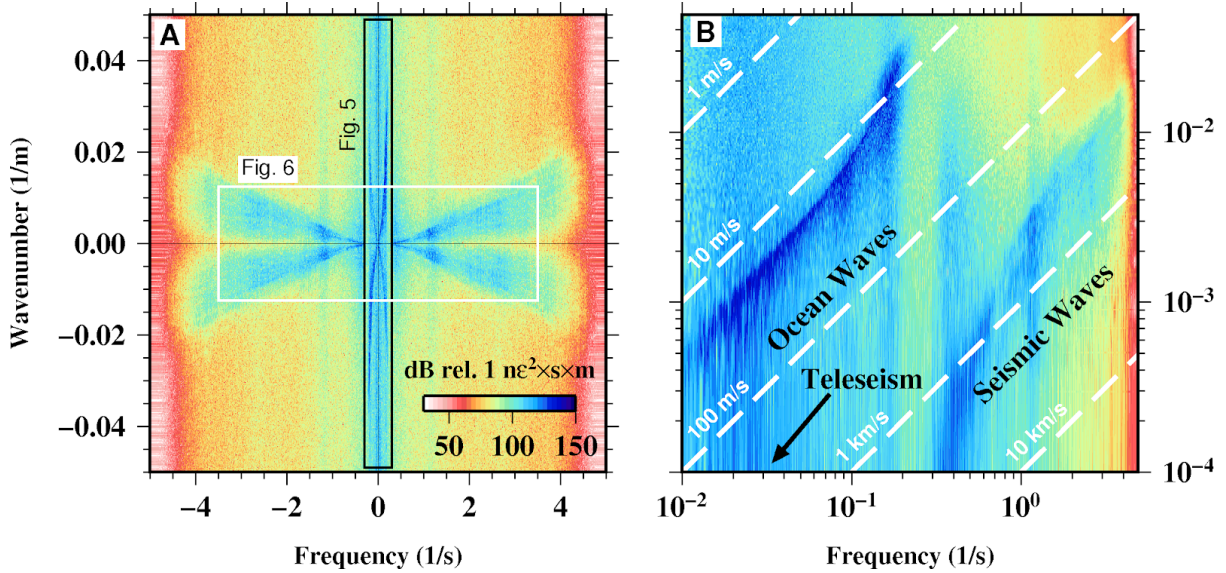

Figure 2: **Separation of ocean and seismic waves** (A) Raw f-k power spectrum of 1 hr of DAS strain data across the full 42-km array. (B) Quadrant 1 (incoming waves) plotted in logarithmic space, showing coherent ocean wave energy at low frequencies and coherent seismic wave energy at high frequencies. Teleseismic waves with near-instantaneous apparent phase velocity appear in the zero-wavenumber bin at low frequencies.

fading of sensitivity along the fiber, as is common in conventional DAS and which would require pre-processing at the expense of bandwidth (see Section 4). Given the quasi-linear geometry of the fiber cable, no corrective algorithms or fiber sectioning methods were applied to compensate cable turns, resulting in slight smearing of energy along the wavenumber axis. In the f-k domain, ocean-related signals appear at low frequencies (<0.7 Hz) with apparent group velocity slower than ∼10 m/s, and are discussed in Section 2.2 (Fig. 2). Seismic surface waves appear at high frequencies (>0.3 Hz) with apparent group velocity faster than ∼300 m/s, and are discussed in Section 2.3 (Fig. 2). Teleseismic body waves from the Fiji earthquake are close to vertically incident and expected to arrive almost simultaneously along the array, hence appearing at wavenumbers lower than can be resolved across a few kilometers aperture. In order to isolate teleseisms, we apply a 2D band-pass filter in the f-k domain between 0.001-1 Hz and 0-0.002 m^{-1} in the first and third quadrants (corresponding to energy propagating land-ward across the array from the north/west; Fig. S2), stack waveforms across a 5-km array segment to form a beam trace, and finally apply a range of bandpass filters to the beam trace to produce the BDASA waveforms shown in Figure 3 (see Supplementary Material). We compare the BDASA beam trace to nearby broadband seismometer BOST (30-50 km south of BDASA), after rotating the horizontal channels into the mean azimuth of the BDASA and bandpass filtering.

At high frequencies (>0.1 Hz), we recover the PKP phase (∼550 s) and its associated pPKP + sPKP depth phases (∼690 s), the travel times of which correspond well to those recorded on BOST (Fig. 3). The envelopes of the recovered P phases are similar to those from BOST, although the waveforms do not match wiggle by wiggle, as expected for high frequency waves strongly affected by near-surface structures and the water layer. At low frequencies (<0.15 Hz), the background noise is substantially stronger, but we still recover a complex S wavetrain, which exhibits moderate-to-high waveform fidelity when compared with BOST (mean correlation coefficient of 0.6; Fig. 3, Fig. S3). Recovered P and S waveforms are both coherent along the length of the array (Fig. S4). Because the BDASA measures strain across a 10-m gauge length whereas BOST measures particle velocity at a single point, theoretical amplitudes are approximately proportional by a factor of the apparent horizontal slowness for wavelengths longer than twice the gauge length (Wang et al., 2018). For the Fiji earthquake, the ratio of BDASA strain amplitude to BOST particle velocity amplitude does not yield reasonable apparent velocities for the observed phases across any band. Hence, we infer that strain-transfer coupling between the solid earth and the BDASA fiber, a consequence of the fiber casing and installation, is complex. While a $M_w 8.2$ deep earthquake is a rare and particularly large event, body wave energy observed in Belgium at 146.7^o epicentral distance is lower in spectral amplitude than would be expected for regional earthquakes (< 1° epicentral distance) greater than ∼ $M3.5$ (see Supplementary Material). Hence, BDASA clearly exhibits teleseismic and regional seismic monitoring capability, as both P-wave and S-wave travel-times can be

121 recovered across a broad band, and S-wave polarity is robust over the frequencies of interest to global
122 seismology.

2.2   Ocean surface gravity waves

124 In addition to the broad, low-frequency peak associated with Fiji teleseisms, the power spectral
125 densities (PSD) of BDASA channels computed over the full 1-hr strain record exhibit four distinct peaks
126 at 0.09 Hz, 0.18 Hz, 0.36 Hz, and 1.12 Hz (Fig. 4a). Here, we focus primarily on the 0.18 and 0.36
127 Hz peaks. We attribute the 0.18 Hz peak to poroelastic strains induced by the pressure field of ocean
128 surface gravity waves propagating across the array. Globally, surface gravity and infragravity waves
129 between 0.003-3 Hz are excited in oceanic waters by wind-sea interaction. Invoking linear wave theory,
130 the magnitude of the seafloor pressure perturbations beneath a surface gravity wave scales with angular
131 wavenumber k and water depth H as $p_d \propto \text{sech}(kH)$ (e.g. Holthuijsen, 2007). We use the dispersion
132 relation for ocean surface gravity waves, $\omega^2 = gk\text{tanh}(kH)$, to calculate a theoretical p_d along the cable
133 depth profile and fit the Fourier amplitude at 0.18 Hz as a linear function of p_d (see Supplementary
134 Material). We observe a good correspondence between the observed and predicted Fourier amplitude at
135 0.18 Hz with both water depth and distance along the cable (Fig. 4b,c), suggesting that surface gravity
136 waves dominate the data at these frequencies.

137 Our interpretation of surface gravity waves at 0.18 Hz is supported by f-k analysis, which shows
138 strong, coherent energy packets in all four quadrants between 0.01-0.26 Hz with peaks at 0.09 and 0.18
139 Hz and slow phase velocities on the order of 1-10 m/s (Fig. 2b, 5). These energy packets are bounded by a
140 sharp upper edge at slow phase velocities, which we fit by the dispersion relation for surface gravity waves
141 (Fig. 5), representing wave energy propagating axially along the cable. Energy below this edge represents
142 surface gravity waves with faster apparent phase velocity that obey the same dispersion relation but are
143 obliquely incident to the fiber. Using the dispersion relation given above, we map energy from these
144 obliquely incident waves to f-k amplitude as a function of azimuth to quantify the variations in the
145 directional spectrum of the ocean wavefield with distance along the fiber (Fig. 5c; see Supplementary
146 Material). The directional spectra appear lobate because DAS measures the axial component of strain,
147 with a directional sensitivity of approximately $\cos^2\theta$ for longitudinal waves (Martin, 2018), hence low
148 broadside sensitivity.

149 For the segment of the BDASA closest to shore, stronger incoming (land-ward propagating) surface
150 gravity waves occupying f-k quadrants 1 and 3 are observed. The relative strength of outgoing (sea-ward
151 propagating) surface gravity waves occupying f-k quadrants 2 and 4 increases with distance along the
152 cable (Fig. 5). For the last 10 km segment of the array between 30 and 40 km the outgoing and incoming

waves are of approximately equal energy (Fig. 5b). We infer that outgoing waves must be reflected from the bathymetric ridge at 30 km and the sloping seabed approaching the coast (Fig. 1b), and note that such opposing wave groups necessarily interfere to produce a standing wave. In particular, the reflective effect of the bathymetric ridge at 30 km can be clearly observed in the directional spectra (Fig. 5c), where incoming wave energy is amplified relative to outgoing energy on the 20-30 km segment and outgoing energy is amplified relative to incoming energy on the 30-40 km segment.

The directional spectrum of surface gravity waves does not change appreciably over time along the first 30 km of the array. For the last 10 km segment, however, the observed f-k spectrum evolves over time and is asymmetrical, with faster incoming waves and slower outgoing waves (Fig. 5b). We fit this asymmetry with a mean-flow correction to the dispersion relation $(\omega - Uk)^2 = gk\tanh(kH)$, which describes the first-order effect of surface gravity waves propagating in a current, where U is the apparent velocity of the current along the cable (Fig. 5b,d,e). Over the 1-hr record, the strength of the observed current increases gradually from 0.1 to 0.5 m/s apparent velocity in the shore-ward direction. Contemporary methods of ocean current measurement are largely limited to either high-frequency radio observation of surface currents (e.g. Chapron et al., 2005; Paduan and Washburn, 2013) or in-situ observation of current-depth profiles using spatially-sparse moorings, drifters, or ship-board instruments (e.g. MODE Group, 1978; Lumpkin and Pezos, 2007; Wunsch, 2015). Our observation of spatio-temporal variations in current speed is significant because it suggests potential application of ocean-bottom DAS to in-situ measurement and monitoring of ocean currents by exploiting models of wave interaction with heterogeneous currents (e.g. Huang et al., 1972) to recover high-resolution spatial (and potentially even depth-dependent) variations in current speed along an array.

2.3   Scholte waves and microseism generation

Unlike the 0.18 Hz energy peak, the 0.36 Hz peak observed in the BDASA PSD is almost invariant with depth and is not adequately described by the pressure-depth scaling of ocean surface gravity waves (Fig. 4c). Instead, the Fourier amplitude at 0.36 Hz increases gradually with distance along the array (Fig. 4b). The cable segment in water depths < 10 m is neglected in this analysis, as the PSD of this region is saturated by incoherent energy across a broad band, likely associated with shoaling of ocean waves. In the f-k domain, we identify a broad energy packet between 0.3 and 3.5 Hz with peaks at 0.36 and 1.12 Hz characterized by phase velocities faster than ∼300 m/s (Fig. 6a). When projected from the frequency-wavenumber domain into frequency-phase velocity space, this high-frequency energy packet exhibits strong dispersion from phase velocities close to the compressional velocity of water (∼1500 m/s) at 0.36 Hz to an asymptotic velocity of ∼250-450 m/s above 1 Hz (Fig. 2b, 6b). Again, in the f-k
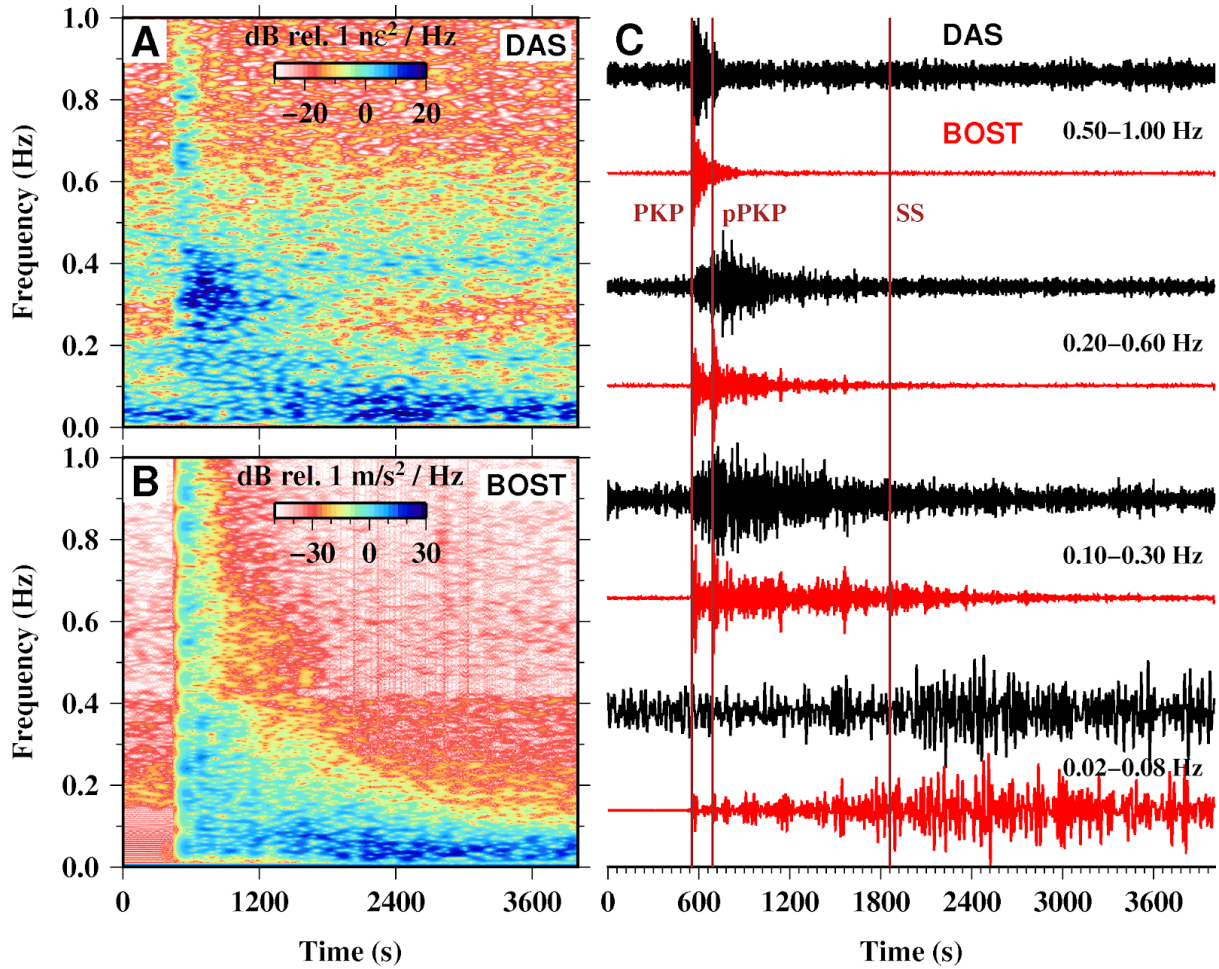
Figure 3: **Teleseismic waveforms** (A) Spectrogram of PSD over time for the f-k filtered and stacked DAS beam trace (black in (C)), showing strong energy between 0-1 Hz around the arrival of the PKP phase around 550 s and below 0.1 Hz following the arrival of the SS phase around 1860 s. (B) Spectrogram for the rotated BOST channel (red in (C)), showing the same major features. (C) Stacked DAS beam trace (black) filtered to various bands between 0.02 and 1 Hz compared with amplitude-normalized particle velocity from broadband station BOST rotated into the mean azimuth of the DAS array (red).

domain the sharp, upper edge of the energy packet corresponds to waves propagating along the cable, and energy appearing below this edge corresponds to waves propagating oblique to the array (Fig. 6a). We consequently attribute the 0.3-3.5 Hz energy to Scholte waves, seismic rock-water interface waves, whose dispersion relation follows the compressional velocity of water at low frequencies and the shear-wave velocity of the shallow sediment layer at high frequencies (Rauch, 1980).

Assuming a true phase velocity of 300 m/s above 1 Hz (the peak velocity in Fig. 6b), we again compute the distribution of f-k amplitude as a function of incident azimuth (Fig. 6c; see Supplementary Material). The directional spectrum of Scholte waves is relatively symmetric along the outer 30 km of the BDASA and shows an azimuthal distribution as would be expected for isotropically propagating or diffuse Scholte waves recorded with DAS (Fig. 6a,c). Scholte waves are observed propagating with subequal-to-equal energy both land-ward and sea-ward across the array (Fig. 6a), hence we infer that these waves must be generated in-situ. We note that the 0.3-3.5 Hz Scholte waves are observed in the 550 s of data preceding the arrival of the first P-wave phases from the Fiji earthquake and therefore must be an independent, local phenomenon.

Globally, seismograms record broadband seismic noise with peaks at 14 and 7 s period, termed microseisms, which have long been attributed to ocean wave sources (e.g. Kedar et al., 2008). Longuet-Higgins [1950] first proposed a mechanism for the double-frequency nature of microseisms, whereby nonlinear interaction of opposing groups of surface gravity waves at one frequency generates a depth-invariant pressure term of second-order magnitude which oscillates at twice the frequency of the surface waves. Hasselmann [1963] expanded this theory to demonstrate that appreciable microseisms are excited only by components of the ocean pressure field that match the phase velocities of the seismic modes of the coupled water-seabed system. In the simplest case, the phase velocity of Longuet-Higgins's second-order pressure term scales as $c = 2\omega/\|\vec{k}_1 + \vec{k}_2\|$ for two plane surface gravity waves with phase $\vec{k}_1 \cdot \vec{x} - \omega t$ and $\vec{k}_2 \cdot \vec{x} - \omega t$. Hence, for opposing waves ($\vec{k}_1 \rightarrow -\vec{k}_2$), c approaches seismic velocities. Based on these theories, we assert that the 0.36 Hz Scholte waves discussed above represent secondary microseism associated with the 0.18 Hz opposing surface gravity wave groups. This is further supported by our observation of gradually increasing Fourier amplitude at 0.36 Hz with distance from the coast (Fig. 4b), as we also observed increasing parity of incoming and outgoing surface gravity waves with distance (Fig. 5) and Longuet-Higgins [1950] predicts that the amplitude of the secondary pressure term is proportional to the product of the amplitudes of the incoming and outgoing ocean wavefield components.

Due to the aperture limits of the BDASA, we are unable to test whether there might be coherent seismic energy at 0.18 Hz, which would represent primary microseism generated in-situ, as demonstrated by the null region (black) in Figure 5b. This aperture limitation also prevents us from describing the 0.09 Hz ocean wave energy and 1.12 Hz Scholte wave energy peaks in detail. Seismic phases associated with
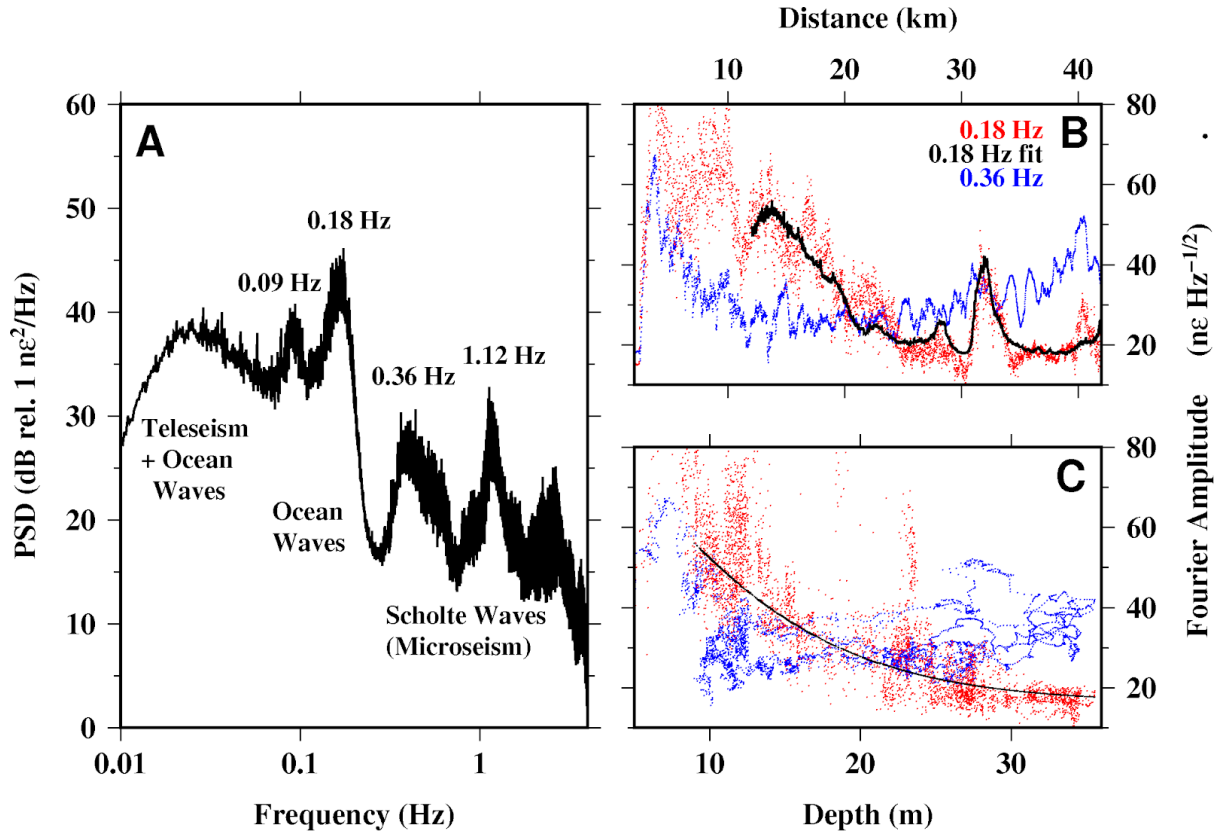
Figure 4: **Comparison of spectra and noise levels** (A) Mean power spectrum of raw DAS strain data over the complete 1 hr record between 35 and 40 km. (B, C) Fourier components of the raw DAS strain spectrum at 0.18 Hz (red) and 0.36 Hz (blue) with noise fit as a function of theoretical pressure at 0.18 Hz (black) plotted as a function of distance along the array (B) and ocean depth (C).

the 0.09 Hz peak would also lie in the null region in Figure 5b. The 1.12 Hz peak and associated high-frequency Scholte wave energy observed up to 3.5 Hz (Fig. 5a) could correspond to a pair of opposing surface gravity wave groups with dominant frequency of 0.55 Hz, which, following the dispersion relation for surface gravity waves, are aliased in our data due to the Nyquist wavenumber of 0.05 m^{-1} for the BDASA. Alternatively, the 1.12 Hz peak could represent a harmonic seismic mode of the subsurface medium, which is excited by resonance, or external environmental noise from an unknown (potentially anthropogenic) source.

3   Discussion and Conclusions

We have presented and analyzed our observations of seismic and ocean waves on an ocean-bottom DAS array offshore Belgium, demonstrating that DAS arrays utilizing existing ocean-bottom fiber optic installations can offer high value seismographic and oceanographic data products. In particular, we successfully recovered both P- and S-phases from the 2018-08-19 Fiji deep earthquake. Rapid, accurate measurement of body wave travel-times is an essential goal of next-generation broadband marine seis-

mology (Lay, 2009) and has motivated many recent advances in ocean-bottom seismic instrumentation (e.g. Hello et al., 2011). Ocean-bottom DAS arrays are an ideal technological solution because they offer real-time telemetry and are intrinsically synchronized, neither of which are easily achievable features of OBS networks. While we were unable to recover robust polarity of high-frequency P-phases, we can expect that ocean-bottom DAS arrays in deep water would have much lower detection thresholds for seismic signals than observed here, as has been demonstrated for OBS (Webb and Crawford, 2010). For an ocean-bottom DAS array, the noise floor can be considered as the superposition of instrumental noise from the DAS interrogator unit and fiber, temperature noise from variations in pore fluid temperature, pressure noise from ocean waves, and seismic noise. The aggressive filtering procedure we applied to recover teleseismic waveforms was necessitated to remove environmental signal, not instrument noise, as coherent signals of physical origin were observed across the full band of interest (0.01-5 Hz). Onshore studies with DAS arrays have found that instrument noise is approximately inversely proportional to frequency with a noise floor no higher than 1 $\mu\varepsilon/\mathrm{Hz}^{1/2}$ at 1 Hz (Williams et al., 2018). Laboratory experiments show that in a stable temperature environment, DAS systems can exhibit a noise floor below 100 $\mathrm{p}\varepsilon/\mathrm{Hz}^{1/2}$ at 1 Hz (Costa et al., 2018). On a DAS array, a temperature perturbation of 1 mK is indistinguishable from a 10 $\mathrm{n}\varepsilon$ strain, so high-frequency temperature fluctuations along the fiber can contribute spurious signals. Water-bottom temperatures may vary on the order of 1 K at tidal periods in the near-shore environment; however, such variability attenuates strongly with depth and is inversely correlated to frequency (e.g. Kaplan et al., 2003; MacDonald et al., 2005). Consequently, instrumental and temperature noise are not limiting factors for most seismological applications, as seen here. In deep water settings, the magnitude of pressure oscillations beneath ocean surface gravity waves, the primary environmental noise which dominates BDASA data between 0.01 and 0.26 Hz, decays exponentially with depth. Therefore, the shallow-water setting of the BDASA actually represents a 'worst case' environment for recording teleseismic events (Webb, 1998; Webb and Crawford, 2010), and thus our ability to recover both P- and S-phases is particularly significant.

Compared to traditional OBS deployments, another advantage of DAS is the number and density of stations. Utilizing hundreds of stations from any segment of the array we were able to apply array-based processing in order to distinguish seismic and ocean signals based on their phase information. So-called "large N" deployments permit low detection thresholds for small earthquakes, precise location of earthquakes, low uncertainty in travel-time measurements, and high-resolution imaging studies (e.g. Rost and Thomas, 2002; Nakata et al., 2015; Li and Zhan, 2018). Further, we have demonstrated that large-N ocean-bottom networks open up new possibilities in studying ocean wave phenomena and microseism generation. The vast majority of studies examining the physics of ocean microseism generation have been limited to remote observation of radiated energy on terrestrial broadband networks (e.g. Friedrich et al.,
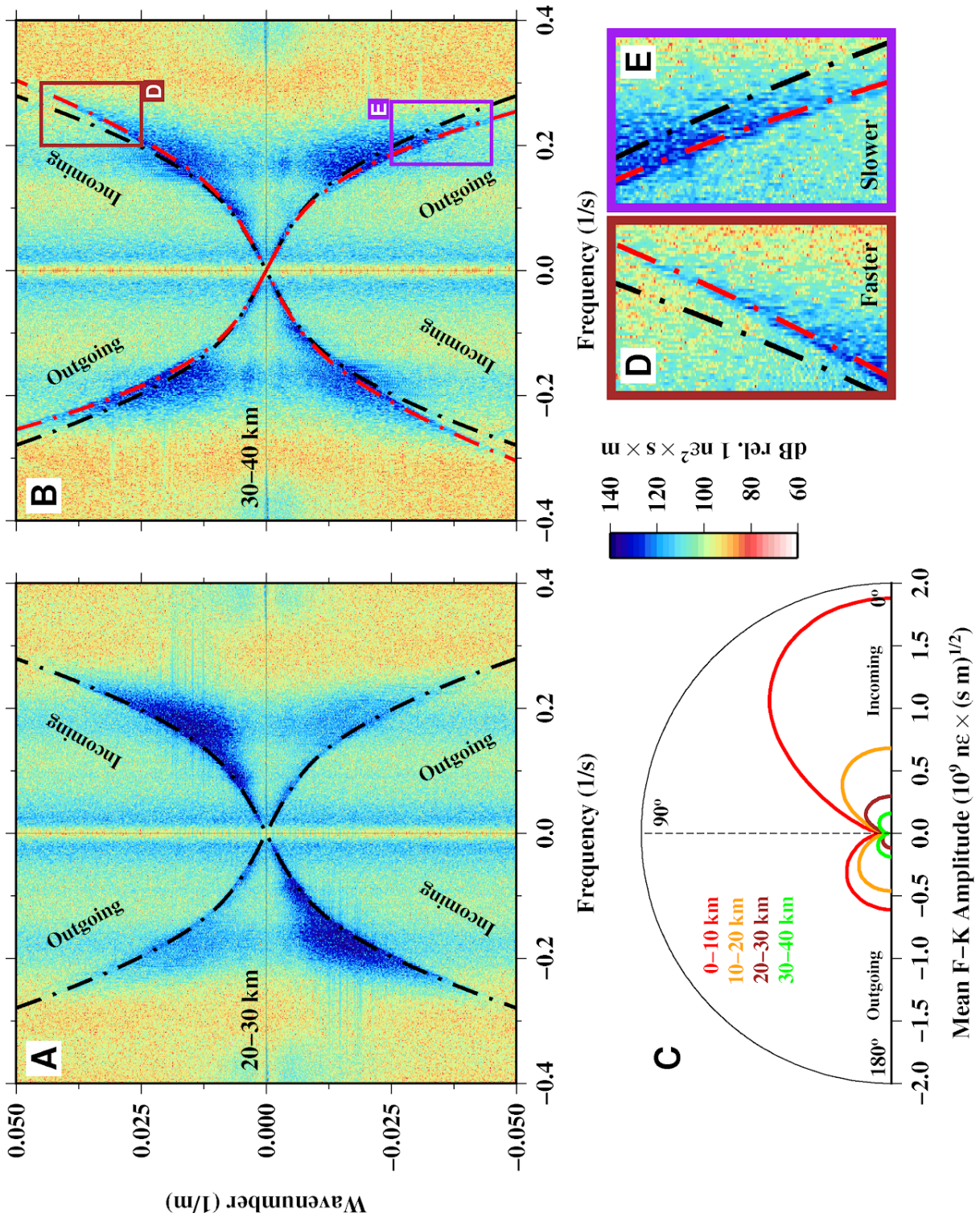
Figure 5: **Ocean surface gravity wave dispersion** (A) Raw DAS f-k spectrum calculated over 10 min between 20 and 30 km with the theoretical ocean surface gravity wave dispersion relation evaluated at H = 25 m (black). (B) Same as (A) but for 30-40 km along the array with the theoretical ocean surface gravity wave dispersion relation modified with a mean-flow term evaluated at H = 25 m and U = 0.5 m/s (red). (C) Mean f-k amplitude as a function of azimuth calculated between 0.05 and 0.25 Hz using the surface gravity wave dispersion relation for four 10-km segments of the BDASA over 10 minutes. Note that DAS measures axial strain and is therefore less sensitive to broadside waves (∼90° incident azimuth). (D), (E) Insets to (B) exhibiting the difference between the mean-flow corrected (red) and uncorrected (black) dispersion relations.

1998; Bromirski, 2001; Kedar et al., 2008; Traer et al., 2012). The few studies utilizing ocean-bottom instrumentation to correlate ocean-wave phenomena with microseism in-situ have been restricted by small network size, effectively resulting in measurements of microseism direction and intensity at a single point with or without simultaneous ocean wave information, and have had mixed success in validating theoretical models (Bradner et al., 1965; Goodman et al., 1989; Dorman et al., 1993; Kibblewhite and Wu, 1993; Nye and Yamamoto, 1994; Bromirski et al., 2005). Simultaneous observation of ocean pressure variations and seismic noise across several thousand channels on ocean-bottom DAS arrays of arbitrary geometry permits reconstruction of the full surface gravity wave and Scholte wave fields, as shown here, and, with the addition of a time-lapse component to future surveys, offers a leap forward in our ability to study microseism and its source processes.

However, several technological challenges still remain before DAS systems can complement or even replace BBOBS on a global scale. Foremost is the axial (single-component) directional sensitivity of DAS. Though work with helically wound optical fibers offering multi-component DAS sensitivity is underway (Hornman, 2017), modern BBOBS already provide four-component recording capability with the same state-of-the-art instruments used in terrestrial networks. We noted that teleseismic waveforms recovered from the BDASA did not exhibit coherent strain amplitude when compared with particle velocity at BOST, suggesting that the mechanics of strain transfer from the solid earth across the cable housing and into the optical fiber are complex and deserve further study (Mellors et al., 2018). In the laboratory, DAS exhibits a linear frequency response, resulting in correct amplitude and distortion free waves (Jousset et al., 2018; Lindsey et al., 2019), hence amplitude preservation may be currently limited by installation conditions and not by the DAS technology itself. Finally, ocean-bottom DAS deployments are not presently possible in remote oceanic locations. Most commercial DAS systems and laboratory measurements claim operation across up to 50 km of fiber, with sensitivity decreasing along the fiber due to optical attenuation. With the use of more complex pulse formats or distributed amplification, the sensing range can be extended to 70-100 km (Fernández-Ruiz et al., 2016; Martins et al., 2015; Pastor-Graells et al., 2017) with a more even distribution of sensitivity along the fiber, while still using a standard telecom fiber installation. In principle, longer distances can be achieved with complex dedicated fiber installations and power supply along the fiber link (via use of optical repeaters (Kim et al., 2001, Gyger et al., 2014) and/or multiple stage distributed amplification (Wang et al., 2014, Martins et al., 2015)), but the impact on the cost and DAS sensitivity means that such systems are not currently practical.
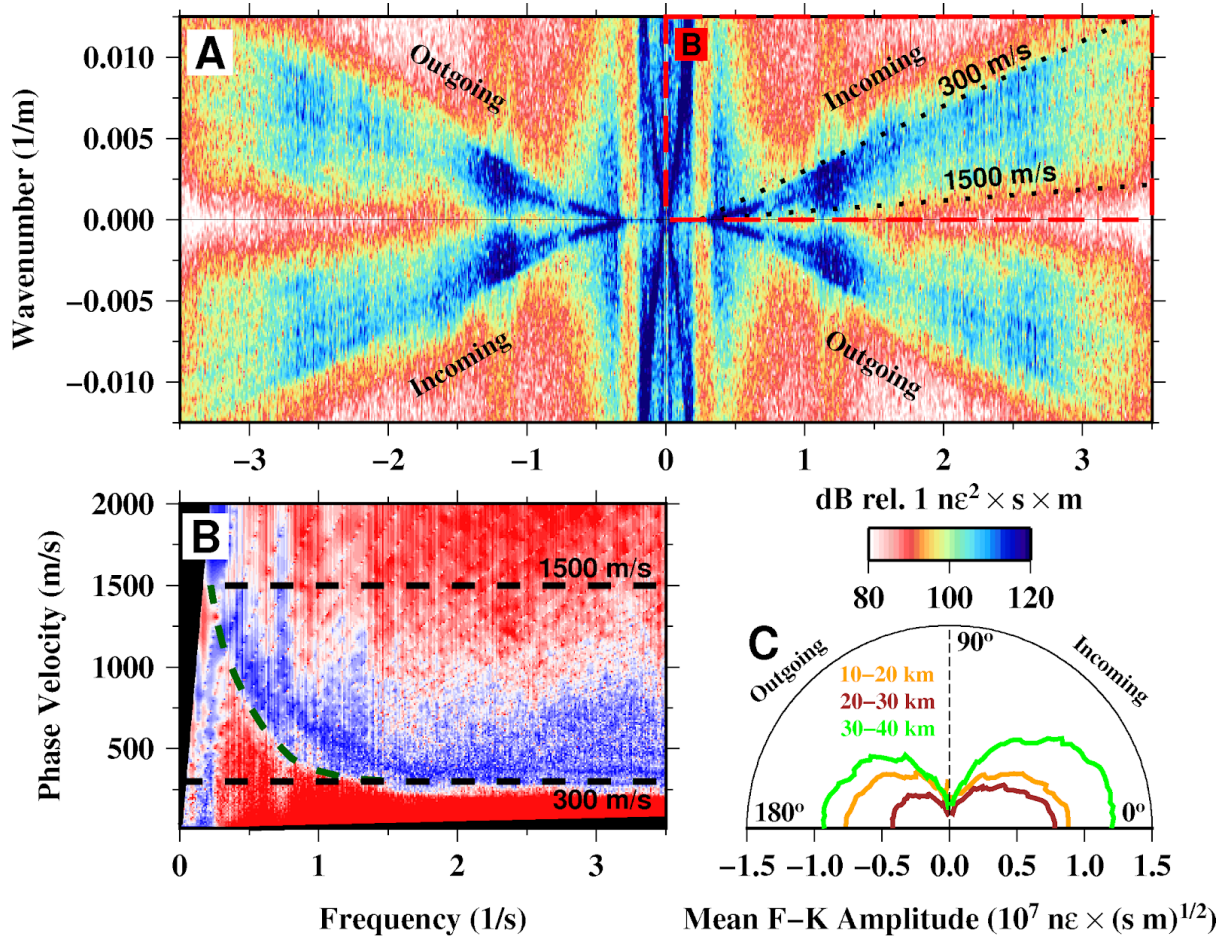
Figure 6: **Scholte wave symmetry and dispersion** (A) One hour of raw DAS strain data from 35-40 km of the array transformed into the f-k domain showing symmetric incoming and outgoing seismic phases between 0.3 and 3.5 Hz. (B) Data from quadrant 1 of (A) projected into phase velocity space showing coherent dispersion from ¿1500 m/s at 0.36 Hz to ~300 m/s above 1 Hz. An approximate dispersion curve is sketched in green. Each frequency bin is normalized, and the black triangles show null regions. (C) Mean f-k amplitude as a function of azimuth calculated between 1.5 and 3.5 Hz by assuming no dispersion (see (B)) and a true Scholte wave velocity of 300 m/s. The theoretical azimuthal sensitivity of DAS to Scholte waves is approximately $\cos^2\theta$ for our acquisition parameters (Martin, 2018).

4 Methods

A chirped-pulse DAS (Pastor-Graells et al., 2016) was used for the interrogator system. In comparison with conventional DAS systems, chirped-pulse DAS offers high signal-to-noise ratio (SNR) and low variations in sensitivity along the fiber (Pastor-Graells et al., 2017, Costa et al., 2018, Fernández-Ruiz et al., 2018a). The key of its performance lies in the use of a linearly chirped probe pulse for the time-domain interrogation. Temperature or strain perturbations around the fiber affect its refractive index, which in turn slightly alters the central wavelength of the propagating light. An appropriately high linear chirp in the probe pulse (i.e., that inducing a spectral content much higher than the spectral content of the transform limited pulse) induces a local wavelength-to-time mapping arisen from the temporal far-field condition (Goodman, 1994). Hence, variations in the central wavelength of the propagating light translate into temporal shifts in the trace at the particular location of the perturbation. The perturbation is then quantified by a time-delay estimation process via local trace-to-trace correlations over temporal windows similar to the probe pulse width.

The principle of operation of chirped-pulse DAS substantially improves the performance of the sensor over conventional DAS schemes. First, strain perturbations can be properly quantified by simply using direct detection. This contrasts with the conventional case, in which it is necessary to detect the trace optical phase for that purpose. Avoiding phase detection brings important advantages. Coherent detection imposes stringent requirement in the coherence length of the laser source, as it limits the DAS operation range due to the need for beating with a local oscillator. In chirped-pulse DAS, the coherent length of the probe laser can be relaxed, in principle simply requiring it to be higher than the pulse width, with almost no detrimental effect on the acoustic SNR (Fernández-Ruiz et al., 2018b). Polarization fading is not observed in chirped-pulse DAS. More importantly, sensitivity of conventional DAS completely fades in certain points along the fiber (acoustic SNR <1 in up to 6% of fiber locations considering a healthy-SNR optical trace) due to the impossibility of maintaining the phase reference in low intensity trace regions caused by its interferometric nature. Those 'blind spots' need to be corrected using complex post-processing techniques or multi-wavelength measurements (Chen et al., 2017), typically at the expense of sensing bandwidth and higher measurements times. Chirped-pulse DAS, however, shows no fading sensitivity, enabling the "raw" strain signal as measured by the DAS to be directly processed without using any denoising/smoothing algorithm. This steady sensitivity has particular impact on the subsequent 2D processing applied to isolate seismic events from other sources, since all points are captured with similar noise/sensitivity along the whole fiber length (>40 km) (Fernández-Ruiz et al., 2018a). In this study, we observed DAS sensitivity variation along the 42-km fiber lower than 3 dB. This is in contrast with the typical SNR variations observed in traditional DAS systems, where a variance of >18

dB in the SNR distribution is expected over a few thousand channels (Fernández-Ruiz et al., 2018a).

The optical resolution (or gauge length) and channel spacing of the employed sensor were both 10 m (equivalent to one seismometer placed very 10 m, measuring distributed strain over a length of 10 m), totaling 4192 channels over 42 km. Each channel was sampled at 1 kHz and later downsampled to 10 Hz in order to reduce the dataset size.

Acknowledgements

Author Contributions

E.F.W., M.R.F.R., and H.F.M. carried out data analysis and wrote the manuscript; R.M. and R.V. acquired the data; Z.Z. and M.G.H. advised data analysis and edited the manuscript.

References

J.B. Ajo-Franklin, S. Dou, N.J. Lindsey, I. Monga, C. Tracy, M. Robertson, C. Ulrich, B. Freifeld, T. Daley, and X.S. Li. Using dark fiber and distributed acoustic sensing for near-surface characterization and broadband seismic event detection. *Scientific Reports*, 9(1):1328, 2019.

J. Berger, G. Laske, J. Babcock, and J. Orcutt. An ocean bottom seismic observatory with near real-time telemetry. *Earth and Space Science*, 3:66–77, 2016.

H. Bradner, J.G. Doods, and R.E. Foulks. Investigation of microseism sources with ocean-bottom seismometers. *Geophysics*, 30(4), 1965.

P.D. Bromirski. Vibrations from the "perfect storm". *Geochemistry, Geophysics, Geosystems*, 2(7), 2001.

356   P.D. Bromirski, F.K. Duennebier, and R.A. Stephen. Mid-ocean microseisms. *Geochemistry, Geophysics,*
357   *Geosystems*, 6(4), 2005.

358   B. Chapron, F. Collard, and F. Ardhuin. Direct measurements of ocean surface velocity from space:
359   Interpretation and validation. *J. Geophys. Res.: Oceans*, 110(C7):C07008, 2005.

360   D. Chen, Q. Lui, and Z. He. Phase-detection distributed fiber-optic vibration sensor without fading-noise
361   based on time-gated digital ofdr. *Optics Express*, 25(7):8315–8325, 2017.

362   L. Costa, H.F. Martins, S. Martin-Lopez, M.R. Fernández-Ruiz, and M. Gonzalez-Herraez. Reaching
363   pε/hz sensitivity in a distributed optical fiber strain sensor. In *Optical Fiber Sensors Conference*, page
364   TuD3, Lausanne, Switzerland, 2018.

365   D. Dolenc, B. Romanowicz, D. Stakes, P. McGill, and D. Neuhauser. Observations of infragravity waves
366   at the monterey ocean bottom broadband station (mobb). *Geochemistry, Geophysics, Geosystems*, 6
367   (9), 2005.

368   L.M. Dorman, A.E. Schreiner, L.D. Bibee, and J.A. Hildebrand. Deep-water seafloor array observations
369   of seismo-acoustic noise in the eastern pacific and comparisons with wind and swell. In *Natural Physical*
370   *Sources of Underwater Sound*, pages 165–174, Springer, New York, 1993.

371   M. R. Fernández-Ruiz, H. F. Martins, J. Pastor-Graells, S. Martin-Lopez, and M. Gonzalez-Herraez.
372   Phase-sensitive otdr probe pulse shapes robust against modulation-instability fading. *Optics Letters*,
373   41(24):5756–5759, 2016.

374   M. R. Fernández-Ruiz, H. F. Martins, L. Costa, S. Martin-Lopez, and M. Gonzalez-Herraez. Steady-
375   sensitivity distributed acoustic sensors. *Journal of Lightwave Technology*, 36(23):5690–5696, 2018a.

376   M. R. Fernández-Ruiz, J. Pastor-Graells, H. F. Martins, A. Garcia-Ruiz, S. Martin-Lopez, , and
377   M. Gonzalez-Herraez. Laser phase-noise cancellation in chirped-pulse distributed acoustic sensing.
378   *Journal of Lightwave Technology*, 36(4):979–985, 2018b.

379   D.W. Forsyth, S.C. Webb, L.M. Dorman, and Y. Shen. Phase velocities of rayleigh waves in the melt
380   experiment on the east pacific rise. *Science*, 280:1235–1238, 1998.

381   A. Friedrich, F. Krueger, and K. Klinge. Ocean-generated microseismic noise located with the gräfenberg
382   array. *Journal of Seismology*, 2(1), 1998.

383   D. Frye, J. Ware, M. Grund, J. Partan, P. Koski, S. Singh, L. Freitag, J. Collins, and R. Dietrick.
384   An acoustically-linked deep-ocean observatory. In *Oceans 2005–Europe, vol. 2*, pages 969–974, Brest,
385   France, 2005.

A. Goertz and A. Wuestefeld. Real-time passive monitoring with a fibre-optic ocean bottom array. *First Break*, 36:55–61, 2018.

D. Goodman, T. Yamamoto, M. Trevorrow, C. Abbott, A. Turgut, M. Badiey, and K. Ando. Directional spectra observations of seafloor microseisms from an ocean-bottom seismometer array. *Journal of the Acoustical Society of America*, 86(2309), 1989.

J.W. Goodman. *Introduction to Fourier Optics*. McGraw-Hill, 1994.

F. Gyger, E. Rochat, S. Chin, and L. Thévenaz. Extending the sensing range of brillouin optical time-domain analysis up to 325 km combining four optical repeaters. *Proceedings of SPIE*, page 9157Q, 2014.

K. Hasselmann. A statistical analysis of the generation of microseisms. *Reviews of Geophysics*, 1(2):177–210, 1963.

Y. Hello, A. Oge, A. Sukhovich, and G. Nolet. Modern mermaids: New floats image the deep earth. *Eos Trans. AGU*, 92(40):337–338, 2011.

L.H. Holthuijsen. *Waves in Oceanic and Coastal Waters*. Cambridge University Press, 2007.

J.C. Hornman. Field trial of seismic recording using distributed acoustic sensing with broadside sensitive fibre-optic cables. *Geophysical Prospecting*, 65(1):35–46, 2017.

N.E. Huang, D.T. Chen, C.C. Tung, and J.R. Smith. Interactions between steady non-uniform currents and gravity waves with applications for current measurements. *Journal of Physical Oceanography*, 2:420–431, 1972.

A. Ito, H. Sugioka, D. Suetsugu, H. Shiobara, T. Kanazawa, and Y. Fukao. Detection of small earthquakes along the pacific-antarctic ridge from t-waves recorded by abyssal ocean-bottom observatories. *Mar. Geophys. Res.*, 33:229–238, 2012.

P. Jousset, T. Reinsch, T. Ryberg, H. Blanck, A. Clarke, R. Aghayev, G.P. Hersir, J. Henninges, M. Weber, and C.M. Krawczyk. Dynamic strain determination using fiber-optic cables allows imaging of seismological and structural features. *Nat. Comm.*, 9(1):2509, 2018.

D.M. Kaplan, J.L. Largier, S. Navarrete, R. Guinez, and J.C. Castilla. Large diurnal temperature fluctuations in the nearshore water column. *Estuarine and Coastal Shelf Science*, 57:385–398, 2003.

S. Kedar, M. Longuet-Higgins, F. Webb, N. Graham, R. Clayton, and C. Jones. The origin of deep ocean microseisms in the north atlantic ocean. *Proceedings of the Royal Society A*, 464:777–793, 2008.

A.C. Kibblewhite and C.Y. Wu. A description of the ulf acoustic noise field in the ocean. In *Natural Physical Sources of Underwater Sound*, pages 189–202, Springer, New York, 1993.

P. Kim, H. Yoon, J. Seo, K. Jeong, K. Ryoo, and K. Lee. Novel in-service supervisory system using otdr for long-haul wdm transmission link including cascaded in-line edfas. *IEEE Photonics Technology Letters*, 13(10):1136–1138, 2001.

T. Lay, ed. Seismological grand challenges in understanding earth's dynamic systems. In *Report to the National Science Foundation*, IRIS Consortium, 2009.

Z. Li and Z. Zhan. Pushing the limit of earthquake detection with distributed acoustic sensing and template matching: a case study at the brady geothermal field. *Geophys. J. Int*, 215(3):1583–1593, 2018.

N.J. Lindsey, E.R. Martin, D.S. Dreger, B. Freifeld, S. Cole, S.R. James, B.L. Biondi, and J.B. Ajo-Franklin. Fiber-optic network observations of earthquake wavefields. *Geophys. Res. Lett.*, 44(23): 11792–11799, 2017.

N.J. Lindsey, H. Rademacher, D.S. Dreger, A. Titov, and J.B. Ajo-Franklin. How broadband is das? two empirical evaluations of instrument response. In *Seismological Society of America Annual Meeting 2019 Technical Sessions*, 2019.

M.S. Longuet-Higgins. A theory of the origin of microseisms. *Phil. Trans. Roy. Soc. A*, 243(857):1–35, 1950.

R. Lumpkin and M. Pezos. Measuring surface currents with surface velocity program drifters: the instrument, its data, and some recent results. *Lagrangian analysis and prediction of coastal and ocean dynamics*, pages 39–67, 2007.

I.R. MacDonald, L.C. Bender, M. Vardaro, B. Bernard, and J.M. Brooks. Thermal and visual time-series at a seafloor gas hydrate deposit on the gulf of mexico slope. *Earth and Planet. Sci. Lett.*, 233:45–59, 2005.

G. Marra, C. Clivati, R. Luckett, A. Tampellini, J. Kronjager, L. Wright, A. Mura, F. Levi, S. Robinson, A. Xuereb, B. Baptie, and D. Calonico. Ultrastable laser interferometry for earthquake detection with terrestrial and submarine cables. *Science*, 361:486–490, 2018.

E.R. Martin. *Passive imaging and characterization of the subsurface with distributed acoustic sensing*. Ph.D. Thesis, Dept. of Geophysics, Stanford University, Stanford, CA, 2018.

H. F. Martins, S. Martin-Lopez, P. Corredera, J. D. Ania-Castañon, O. Frazão, and M. Gonzalez-Herraez. Distributed vibration sensing over 125 km with enhanced snr using phi-otdr over a urfl cavity. *Journal of Lightwave Technology*, 33(12):2628–2632, 2015.

A. Mateeva, J. Mestayer, B. Cox, D. Kiyashchenko, P. Wills, J. Lopez, S. Grandi, K. Hornman, P. Lumens, A. Franzen, and D. Hill. Advances in distributed acoustic sensing (das) for vsp. In *SEG Technical Program Expanded Abstracts 2012*, pages 1–5, 2012.

J.J. McGuire, T. Plank, and et al. The sz4d initiative: Understanding the processes that underlie subduction zone hazards in 4d. In *Vision Document Submitted to the National Science Foundation*, The Iris Consortium, 2017.

R.J. Mellors, C. Yu, C. Mart, C. Sherman, P. Pax, K. Fisher, G. Allen, M. Messerly, J. Morris, and F.J. Ryerson. Understanding distributed fiber optic sensing response for modeling of signals. In *SEG Technical Program Expanded Abstracts 2018*, pages 4679–4682, 2018.

J. Mestayer, B. Cox, P. Wills, D. Kiyashchenko, J. Lopez, M. Costello, S. Bourne, G. Ugueto, R. Lupton, G. Solano, and D. Hill. Field trials of distributed acoustic sensing for geophysical monitoring. In *SEG Technical Program Expanded Abstracts 2011*, pages 4253–4257, 2011.

MODE Group. The mid-ocean dynamics experiment. *Deep Sea Research*, 25:859–910, 1978.

N. Nakata, J.P. Chang, J.F. Lawrence, and P. Boue. Body wave extraction and tomography at long beach, california, with ambient-noise interferometry. *J. Geophys. Res.: Solid Earth*, 120(2):1159–1173, 2015.

T. Nye and T. Yamamoto. Field test of buried ocean-wave directional spectrometer system. *Journal of Waterway, Port, Coastal, and Ocean Engineering*, 120(5), 1994.

J.D. Paduan and L. Washburn. High-frequency radar observations of ocean surface currents. *Ann. Rev. Marine Sci.*, 5:115–136, 2013.

T. Parker, S. Shatalin, and M. Farhadiroushan. Distributed acoustic sensing - a new tool for seismic applications. *First Break*, 32:61–69, 2014.

J. Pastor-Graells, H. F. Martins, A. Garcia-Ruiz, S. Martin-Lopez, and M. Gonzalez-Herraez. Single-shot distributed temperature and strain tracking using direct detection phase-sensitive otdr with chirped pulses. *Optics Express*, 24(12):13121–13133, 2016.

J. Pastor-Graells, J. Nuño, M. R. Fernández-Ruiz, A. Garcia-Ruiz, H. F. Martins, S. Martin-Lopez, and M. Gonzalez-Herraez. Chirped-pulse phase-sensitive reflectometer assisted by first-order raman amplification. *Journal of Lightwave Technology*, 35(21):4677–4683, 2017.

D. Rauch. Seismic interface waves in coastal waters: a review. In *SACLANTCEN Report SR 42*, 1980.

S. Rost and C. Thomas. Array seismology: methods and applications. *Reviews of Geophysics*, 40(3): 2–1–2–27, 2002.

M. Shinohara, T. Yamada, K. Nakahigashi, S. Sakai, K. Mochizuki, K. Uehira, Y. Ito, R. Azuma, Y. Kaiho, T. No, H. Shiobara, R. Hino, Y. Murai, H. Yakiwara, T. Sato, Y. Machida, T. Shinbo, T. Isse, H. Miyamachi, K. Obana, N. Takahashi, S. Kodaira, Y. Kaneda, K. Hirata, S. Yoshikawa, K. Obara, T. Iwasaki, and N. Hirata. Aftershock observation of the 2011 off the pacific coast of tohoku earthquake by using ocean bottom seismometer network. *Earth Planets Space*, 63:835–840, 2011.

D. Suetsugu and H. Shiobara. Broadband ocean-bottom seismology. *Annu. Rev. Earth Planet. Sci.*, 42: 27–43, 2014.

D. Suetsugu, M. Shinohara, E. Araki, T. Kanazawa, K. Suyehiro, T. Yamada, K. Nakahigashi, H. Shiobara, H. Sugioka, K. Kawai, and Y. Fukao. Mantle discontinuity depths beneath the west philippine basin from receiver function analysis of deep-sea borehole and seafloor broadband waveforms. *Bull. Seismol. Soc. Am.*, 95:1947–1956, 2005.

H. Sugioka, T. Okamoto, T. Nakamura, Y. Ishihara, A. Ito, K. Obana, M. Kinoshita, K. Nakahigashi, M. Shinohara, and Y. Fukao. Tsunamogenic potential of the shallow subduction plate boundary inferred from slow seismic slip. *Nat. Geosci.*, 5:414–418, 2012.

Y.J. Tan, M. Tolstoy, F. Waldhauser, and W.S.D Wilcock. Dynamics of a sea-floor spreading episode at the east pacific rise. *Nature*, 540:261–265, 2016.

D.R. Toomey, W.S.D. Wilcock, S.C. Solomon, W.C. Hammond, and J.A. Orcutt. Mantle seismic structure beneath the melt region of the east pacific rise from p and s wave tomography. *Science*, 280: 1224–1227, 1998.

J. Traer, P. Gerstoft, P.D. Brominski, and P.M. Shearer. Microseisms and hum from ocean surface gravity waves. *Journal of Geophysical Research: Solid Earth*, 117(B11307), 2012.

H.F. Wang, X. Zeng, D.E. Miller, D. Fratta, K.L. Feigl, C.H. Thurber, and R.J. Mellors. Ground motion response to an ml 4.3 earthquake using co-located distributed acoustic sensing and seismometer arrays. *Geophys. J. Int.*, 213(3):2020–2036, 2018.

Z. N. Wang, J. J. Zeng, J. Li, M. Q. Fan, H. Wu, F. Peng, L. Zhang, Y. Zhou, and Y. J. Rao. Ultra-long phase-sensitive otdr with hybrid distributed amplification. *Optics Letters*, 39(20):5866–5868, 2014.

S.C. Webb. Broadband seismology and noise under the ocean. *Reviews of Geophysics*, 36(1):105–142, 1998.

S.C. Webb and W.C. Crawford. Shallow-water broadband obs seismology. *Bull. Seis. Soc. Am.*, 100(4): 1770–1778, 2010.

S.C. Webb, T.K. Deaton, and J.C. Lemire. A broadband ocean-bottom seismometer system based on a 1-hz natural period geophone. *Bull. Seismol. Soc. Am.*, 91:304–312, 2001.

C. Wunsch. *Modern observational physical oceanography.* Princeton University Press, 2015.

C. Yu, Z. Zhan, N.J. Lindsey, J.B. Ajo-Franklin, and M. Robertson. The potential of das in teleseismic studies: Insights from the goldstone experiment. *Geophys. Res. Lett.*, 46, 2019.